Moiré nematic phase in twisted double bilayer graphene

Carmen Rubio-Verdú[1]*, Simon Turkel[1]*, Larry Song[1], Lennart Klebl[2], Rhine Samajdar[3], Mathias S. Scheurer[3,4], Jörn W. F. Venderbos[5,6], Kenji Watanabe[7], Takashi Taniguchi[8], Héctor Ochoa[1], Lede Xian[9], Dante M. Kennes[2,9], Rafael M. Fernandes[10], Ángel Rubio[9,11,12], Abhay N. Pasupathy[1†]

[1]Department of Physics, Columbia University, New York, NY 10027, USA
[2]Institute for Theory of Statistical Physics, RWTH Aachen University, and JARA Fundamentals of Future Information Technology, 52062 Aachen, Germany
[3]Department of Physics, Harvard University, Cambridge, MA 02138, USA
[4]Institute for Theoretical Physics, University of Innsbruck, A-6020 Innsbruck, Austria
[5]Department of Physics, Drexel University, Philadelphia, PA 19104, USA
[6]Department of Materials Science and Engineering, Drexel University, Philadelphia, PA 19104, USA
[7]Research Center for Functional Materials, National Institute for Materials Science, 1-1 Namiki, Tsukuba 305-0044, Japan
[8]International Center for Materials Nanoarchitectonics, National Institute for Materials Science, 1-1 Namiki, Tsukuba 305-0044, Japan
[9]Max Planck Institute for the Structure and Dynamics of Matter, Center for Free Electron Laser Science, 22761 Hamburg, Germany
[10]School of Physics and Astronomy, University of Minnesota, Minneapolis, MN 55455, USA
[11]Center for Computational Quantum Physics (CCQ), The Flatiron Institute, New York, NY 10010, USA
[12]Nano-Bio Spectroscopy Group, Departamento de Física de Materiales, UPV/EHU, 20018 Donostia, Spain

* These authors contributed equally to this work.
† Corresponding author: apn2108@columbia.edu

Graphene moiré superlattices display electronic flat bands. At integer fillings of these flat bands, energy gaps due to strong electron-electron interactions are generally observed. However, the presence of other correlation-driven phases in twisted graphitic systems at non-integer fillings is unclear. Here, we report the existence of threefold rotational symmetry breaking in twisted double bilayer graphene. Using spectroscopic imaging over large and uniform areas to characterize the direction and degree of C_3 symmetry breaking, we find it to be prominent only at energies corresponding to the flat bands and nearly absent in the remote bands. We demonstrate that the magnitude of the rotational symmetry breaking does not depend on the degree of the heterostrain or the displacement field, being instead a manifestation of an interaction-driven electronic nematic phase. We show that the nematic phase is a primary order that arises from the normal metal state over a wide range of doping away from charge. Our modelling suggests that the nematic instability is not associated with the local scale of the graphene lattice, but is an emergent phenomenon at the scale of the moiré lattice.

Clear signatures of correlated electronic phases have been observed in magic-angle twisted bilayer graphene (MATBG)[1–8], twisted double bilayer graphene (TDBG)[9–14] and trilayer rhombohedral graphene on hexagonal boron nitride (hBN) [15,16]. In all of these cases, the moiré pattern gives rise to flat bands near the Fermi level. The correlated phases that have been observed so far are found at integer fillings of the moiré unit cell. Whether other observed electronic phases such as superconductivity are also caused by correlations and how ubiquitous they might be across twisted graphitic systems still remain open questions.

Here we focus on the nematic phase of graphitic moiré systems – a state where the discrete rotational symmetry of the moiré lattice is broken, while translational symmetry is preserved[17,18,19]. Recent STM[4,5,8] and transport[20] experiments on MATBG reported evidence of broken threefold rotational symmetry. Since in several of these experiments nematicity was observed in the presence of preexisting phases, it is not clear whether the observed nematic behavior is a primary instability of the normal metal, or is a secondary order that onsets after the breaking of a different symmetry. In fact, in MATBG, it is challenging for local spectroscopic measurements to disentangle nematic order from effects caused by the significant heterostrain and twist disorder that exists in all MATBG samples studied so far. Finally, it is not known whether broken rotational symmetry is a specific property of MATBG or a more universal feature of twisted graphitic systems. In order to answer these questions, we focus on TDBG, a flat band system that is related but different from MATBG.

Twisted double bilayer graphene is formed by creating a twist angle between two pieces of Bernal-stacked bilayer graphene. Like MATBG, correlated insulating phases have been found in TDBG at integer fillings of the moiré lattice[9–12]. The electronic structure of TDBG does not have a magic angle condition, making its electronic properties less sensitive to twist angle and its spatial variations. Importantly, the increased mechanical stiffness of bilayer graphene relative to monolayer graphene make it significantly easier to produce large-area uniform samples that are strain and disorder free. TDBG therefore provides a more transparent and robust platform than MATBG to investigate the presence of nematic phases, free from extrinsic effects.

Our experiments are conducted on moiré regions of TDBG on hBN using scanning tunneling microscopy (STM) and spectroscopy (STS) at 5.7 K. Fig. 1a shows an STM topograph over a large area of a TDBG sample with a twist angle of 1.05 degrees and a heterostrain value of 0.03 %. Fig. 1b shows a smaller moiré area, where regions of BAAC stacking (bright spots) are surrounded by inequivalent ABAB (Bernal) and ABCA (rhombohedral) domains[21]. The heterostrain occurs between the two bilayers, since strain within a given bilayer would introduce a soliton network not observed

experimentally[22]. Having samples with such twist angle homogeneity and low heterostrain is unprecedented in open-face devices and is crucial to the discussion that follows.

The presence of a large density of states within a narrow energy range of the Fermi level is of central importance to the physics of graphitic moiré systems. Fig. 1c compares STS measurements on each of the three inequivalent high-symmetry stacking configurations at zero doping (i.e. charge neutrality) and zero displacement field. On all three sites, we observe two large peaks in the density of states, one below and one above the Fermi level, corresponding to the valence flat band (VFB) and to the conduction flat band (CFB), respectively. Unlike MATBG, in which the flat bands are restricted to the AA sites, in TDBG they are spread out with varying spectral weights over the entire moiré unit cell. In addition, we observe higher energy peaks corresponding to the remote valence and conduction bands RV_2, RV_1, RC_1 and RC_2 at around -100, -50, +50 and +100 meV, respectively, which arise from the crossing of the parabolic bands of each Bernal bilayer.

We compare our experimental spectra to theoretical calculations of the local density of states (LDOS) in Figs. 1d and 1e. We consider two complementary models: a microscopic tight-binding model[23] (Fig. 1d) and an effective low-energy continuum model[24,25] (Fig. 1e). Experimentally, due to the STM geometry, the LDOS is dominated by the top layer. Therefore, to make comparisons with the experimental data meaningful, we project the LDOS onto the top graphene layer, which is where electrons from the STM tip are most likely to tunnel (details in the Supplementary Information (SI)). Despite some minor differences, the STM spectrum at charge neutrality is very well described by both non-interacting models.

In the absence of heterostrain and applied displacement field, TDBG is characterized by a D_3 symmetry point group, which contains an out-of-plane threefold rotational axis (C_3) and three in-plane twofold rotational axes (C'_2). Shown in Fig. 1f are experimental images of the charge-neutral and zero-field STS LDOS at energies corresponding to the remote and flat bands shown in Fig. 1c. The VFB and CFB are mostly localized on the ABAB moiré sites. Triskelion structures arise at the energies of the remote bands, which are mostly localized on the ABCA sites. At the energy of the second remote bands and above, the STS LDOS is peaked on the BAAC sites. The corresponding theoretical LDOS maps obtained from the tight-binding model are shown in Fig. 1g, displaying remarkable agreement with our experimental maps in Fig. 1f. The fact that all the structures observed in Fig. 1f preserve threefold rotational symmetry shows that extrinsic effects that could break C_3 symmetry such as heterostrain can be neglected.

Our TDBG device's geometry consists of a bias voltage electrode in direct contact with the TDBG flakes that sweeps the energy, and a back-gate electrode separated from the graphene structure by hBN that controls both carrier density and displacement field. Fig. 2a presents gate- and energy-dependent STS maps obtained in the remote and flat bands (black dots in Fig. 2d), over gate voltage values ranging from an almost empty valence band (bottom row) to an almost full conduction band (top row). While the STS LDOS maps of the remote bands are nearly unchanged and retain C_3 symmetry for all gate voltages, the spatial distribution of the flat band STS LDOS changes significantly as a function of gate voltage. Most importantly, the VFB STS LDOS displays pronounced unidirectional stripes at certain values of the gate voltage. This breaking of C_3 symmetry over a well-defined range of energy and gate voltage is the main result of the present work.

The application of a back gate voltage in the STM geometry induces a nonzero charge doping as well as a transverse displacement field[21,26]. Unlike MATBG, the band structure of TDBG is highly sensitive to the presence of an out-of-plane displacement field. Shown in Fig. 2d is the evolution of the spatially averaged (over ABAB, BAAC, and ABCA sites) spectrum as a function of gate voltage. The main effect of sample doping is a rigid shift of the spectra along the energy axis. The displacement field, by contrast, directly modifies the band structure and, therefore, the density of states. We calculated the effect of the displacement field within the continuum model in the presence of a self-consistently screened electric field and found quantitative agreement with experiment (see SI for details). The presence of a displacement field breaks the in-plane C'_2 rotational symmetry but leaves the out-of-plane C_3 rotational symmetry unaltered, and thus cannot explain the unidirectional stripes observed in the experiment. Importantly, for the values of the displacement field used in our experiment, there is no correlated insulating state present, and indeed, we do not see any evidence for an insulating gap in our spectra at the Fermi level. This clearly establishes that the nematic order that we observe is a primary order, i.e., it is an instability of the normal metallic Fermi liquid.

A map that respects C_3 symmetry will look identical when rotated by 120 degrees. We can quantify the degree of C_3 symmetry breaking (i.e. nematicity) by considering differences between a given STS LDOS map and its C_3 rotated counterpart[4]. This measure of anisotropy is superimposed as a color scale on the spectra in Fig. 2d and reveals that the anisotropy is present at doping values between 0.3 and 0.7 filling of the CFB, at energies primarily in the VFB. Shown in Fig. 2b is a spectroscopic image of the STS LDOS in the VFB near half-filling of the CFB, conditions under which the stripes are prominently seen. Overlaid on the image are the moiré lattice high-symmetry site positions. We see

that the stripes connect the ABCA and ABAB regions, running in between the darkened BAAC sites and parallel to one of the moiré crystal axes, shown by the dashed lines in Fig. 2b.

Fig. 2c shows the spectra on each of the three high-symmetry site positions as a function of gate voltage. Here, we draw attention to the spectral shape of the VFB, which is where the stripes are observed. At most gate voltages, the VFB peak's energy (red dots) is identical for the three high-symmetry site positions. However, at the gate voltages where broken C_3 symmetry is observed, the VFB peaks split, appearing ~4 meV further from the Fermi level on the BAAC site than in ABAB and ABCA sites. While our non-interacting calculations capture the spectrum quite well, they fail to describe this site-dependent splitting of the VFB. The fact that the STS LDOS develops stripes only at specific values of energy and doping (oriented along a specific crystallographic direction, see below), combined with the inability of single-particle calculations to describe the LDOS spectra at these energies and doping values, is a strong indication that the observed symmetry breaking is driven by electron-electron correlations.

In order to shed light on the phase diagram of TDBG, we compare our observation of C_3 symmetry breaking with the correlated insulator state reported in transport experiments. For the range of twist angles explored here, transport experiments report well-developed insulating states for displacement field values between 0.18 and 0.35 V/nm at half-filling of the conduction band[11]. Experimentally, our observations of broken C_3 symmetry take place between 0.08 and 0.16 V/nm. We observed similar phenomenology in a second sample at a slightly higher twist angle of 1.1° (see SI). Thus, the existence of a symmetry-broken phase over a broad swath of our parameter space, at values of displacement fields away from the correlated insulator state, indicates that electron-electron interactions are ubiquitous in the phase diagram of TDBG even when insulating phases are absent.

Figs. 3a-b show STS LDOS maps at the energy of the VFB on two overlapping regions of the sample, one near charge neutrality and one near half-filling, respectively. In agreement with what was shown above, nematic behavior is only observed away from charge neutrality. Moreover, the stripe-like pattern extends over hundreds of nanometers, indicating a genuine long-range ordered phase. Shown in the insets of Figs. 3a-b are the corresponding Fast Fourier Transform (FFT) maps. The three moiré Bragg peaks are present at all fillings with varying intensities. No additional peaks besides these three appear, indicating that translational symmetry is preserved, and thereby ruling out a charge-density wave as the origin of the anisotropy. Thus, we conclude that a true nematic phase arises in TDBG.

The anisotropy presented in images such as those in Figs. 3a-b can be analyzed in Fourier space by considering the intensities of the three moiré Bragg peaks as a function of energy and gate voltage, (see Fig. 3c-d). Close to charge neutrality (Fig. 3c), the energy-dependent intensities of the three Bragg peaks remain equal for the whole energy range. However, around half-filling, while the three Bragg peaks have essentially the same intensity across most of the bias range, the peaks split at energies in the VFB, with one of them showing a higher intensity than the other two (see Fig. 3d); in the CFB, they return to equal intensities. The fact that two Bragg peaks in the VFB retain the same intensity while only one of the three is different proves that the nematic director is located along a principal axis of the moiré lattice – otherwise, the three peaks would have three distinct intensities[27].

We can ask whether heterostrain would give rise to similar phenomenology as that observed in the symmetry-broken phase. We consider heterostrain in both the tight-binding and continuum models. The tight-binding heterostrained system does not show the experimentally observed valence band splitting (see Supp. Fig. 4). As simulating large parameter spaces is numerically too expensive for the tight-binding model, we calculated the LDOS in the continuum model following Ref. 28. For each heterostrain magnitude ε and direction ϕ we can examine the Fourier peak intensities of the LDOS as a function of energy. Shown in Fig. 3e are the resulting peak intensities for energies in the VFB and CFB. For most of ε and ϕ values, the three Fourier peaks have three distinct intensities, indicating that symmetry breaking due to heterostrain is, in general, not pointed along a principal moiré axis. Contrarily, in experiments, the observed symmetry breaking in the VFB LDOS is pointed along a principal moiré axis as discussed above. Moreover, the dependence of the peak intensity shows nearly identical contours for both the CFB and VFB LDOS. Strain-induced symmetry breaking is therefore expected to produce similar signatures in Fourier space over wide energy ranges spanning both flat bands. However, experimentally, we observe C_3 broken Fourier peaks intensities only in the VFB and only at specific gate voltages. Fig. 3f shows the continuum model's LDOS in each flat band in the presence of heterostrain. Neither bears resemblance to the experimental images.

The foregoing discussion implies that heterostrain cannot account for the observed symmetry-broken phase within a single particle picture. One might ask whether small strains in either bilayer in the presence of strong interactions would give rise to a magnified anisotropic response - i.e., whether the system possesses a strong nematic susceptibility rather than true nematic order. To investigate this possibility, we study a second sample of TDBG with a similar twist angle but a enhancement in heterostrain (see SI). The fourfold difference in heterostrain magnitude would produce a comparable difference in the strength of the nematic order parameter if the observed

symmetry breaking were a result of external strain. On the contrary, we observe practically no difference in the strength of nematic order between these two samples, as measured by LDOS anisotropy (see SI Sec. 2). The nearly identical anisotropy values in two samples with a fourfold difference in heterostrain demonstrates the insensitivity of the observed nematic order to small lattice distortions, providing direct evidence of nematic order in the sample rather than a strong nematic susceptibility.

Having ruled out heterostrain and displacement fields as possible causes for C_3 symmetry breaking, we investigate whether interactions could promote a spontaneous electronic nematic state. While previous theoretical works have discussed nematicity in MATBG[27,29–37], very few deal with C_3 symmetry breaking in TDBG[29,38]. Ref. 31 studied a general interacting model on a triangular moiré lattice, finding that nematic order is the leading and dominant instability in the phase diagram. Starting from our microscopic tight-binding model at half-filling of the CFB, we add a screened Coulomb repulsion that is cut off at a distance of ~4.9 Å (Fig. 4a). Using both a random phase approximation (RPA) and an unbiased, beyond mean-field functional renormalization group (fRG) approach[39], we find a nematic instability on the moiré scale as the leading symmetry-breaking instability for a wide range of interaction strengths (see SI). This result supports the experimental conclusion of an intrinsic nematic ordering scenario. The nematic instability's influence is manifested as threefold anisotropic features in the LDOS for low energies (Fig. 4b), in agreement with the STS images for the same doping levels.

To gain a better understanding of the underlying mechanisms at play, we complement the RPA and fRG calculations, which demonstrate the existence of a strong effective interaction in the nematic channel in TDBG, by studying the spatial and energetic dependence of the nematic order parameter. We employ the continuum model and write down the most general form of the continuum nematic order parameter in layer, sublattice, valley, and spin space (see SI). Given the large number of quantum numbers, one can write many different nematic order parameters that break the C_3 symmetry of the moiré lattice. Although symmetry enforces all order parameters to be nonzero in the nematic phase, it is interesting to ask whether the experimentally observed features in the STS LDOS point to a dominant one. We consider two opposite limits[38]: a nematic order parameter that breaks C_3 at the scale of the atomic lattice (*graphene nematic*, Fig. 4d), and a nematic order parameter that breaks C_3 symmetry at the scale of the moiré lattice by making its bonds inequivalent (*moiré nematic*, see Fig. 4c). While graphene nematicity is only sensitive to the existence of the moiré lattice because of the imposed interlayer potential, moiré nematicity is insensitive to the local properties of the layers.

In Fig. 4e, we show the resulting LDOS for the noninteracting, moiré nematic, and graphene nematic cases. Only in the case of moiré nematicity the VFB peak at position BAAC splits from the peaks at the other two positions, similar to what is observed experimentally in Fig. 2c and also reproduced by the fully microscopic model. We also included heterostrain in the moiré nematic model and found (Supp. Fig. 6) that not only does it fail to improve the agreement with experiment, but in fact can be inimical to the symmetry-broken order for certain strain orientations. The LDOS images at the energies of the remote and flat bands shown in Figs. 4f-h further reveal that in the case of moiré nematicity, the threefold anisotropy is much more pronounced in the VFB, is smaller but noticeable in the CFB, and is negligible in the remote bands. This can be understood in terms of the layer-distribution of the spectral weight of the wavefunctions[38]: the VFB wave functions have a strong projection on the topmost layer, and since the tunneling occurs mostly onto the top layer in the STM configuration, the LDOS measured in our experiment is the largest for this band; hence, the VFB displays stronger signatures of nematic order than the other bands[38]. In the case of graphene nematicity, the changes in the LDOS are almost imperceptible. The combination of the results from the tight-binding and continuum models suggests that the nematicity observed in TDBG is an emergent instability of the moiré superlattice.

Our experimental study reveals that nematicity is an integral part of the phase diagram of TDBG, being realized in a wide doping range away from charge neutrality. We also observe nematicity in regions of the phase diagram where insulating behavior is not observed, indicating that the nematic order is the primary broken symmetry phase in TDBG that onsets before other phases do. While we do not have direct evidence for nematic behavior coexisting with insulating behavior in this system, our understanding of the observed moiré nematic in TDBG points to its continued presence at higher displacement fields where insulating behavior is observed. This raises interesting questions of the interplay of the nematic order with other order parameters. The moiré-scale breaking of rotational symmetry also indicates that this instability might be generically expected in carbon-free flat band moiré lattices, a subject for future experimental investigation.

1. Cao, Y. *et al.* Correlated insulator behaviour at half-filling in magic-angle graphene superlattices. *Nature* **556**, 80–84 (2018).

2. Cao, Y. *et al.* Unconventional superconductivity in magic-angle graphene superlattices. *Nature* **556**, 43–50 (2018).

3. Yankowitz, M. *et al.* Tuning superconductivity in twisted bilayer graphene. *Science (80-.).* **363**, 1059–1064 (2019).

4. Kerelsky, A. *et al.* Maximized electron interactions at the magic angle in twisted bilayer graphene. *Nature* **572**, 95–100 (2019).

5. Choi, Y. *et al.* Electronic correlations in twisted bilayer graphene near the magic angle. *Nat. Phys.* **15**, 1174–1180 (2019).

6. Sharpe, A. L. *et al.* Emergent ferromagnetism near three-quarters filling in twisted bilayer graphene. **608**, 605–608 (2019).

7. Urgell, C., Watanabe, K., Taniguchi, T., Zhang, G. & Bachtold, A. Superconductors , orbital magnets and correlated states in magic-angle bilayer graphene. *Nature* **574**, 20–23 (2019).

8. Jiang, Y. *et al.* Charge order and broken rotational symmetry in magic-angle twisted bilayer graphene. *Nature* **573**, 91–95 (2019).

9. Shen, C. *et al.* Correlated states in twisted double bilayer graphene. *Nat. Phys.* **16**, 520–525 (2020).

10. Liu, X. *et al.* Spin-polarized Correlated Insulator and Superconductor in Twisted Double Bilayer Graphene. *Nature* **583**, 221-225 (2020)

11. Cao, Y. *et al.* Tunable correlated states and spin-polarized phases in twisted bilayer – bilayer graphene. *Nature* (2020). doi:10.1038/s41586-020-2260-6

12. He, M. *et al.* Tunable correlation-driven symmetry breaking in twisted double bilayer graphene. *Nat. Phys.* **17**, 26-3*0* (2021).

13. Liu, X. *et al.* Spectroscopy of a Tunable Moiré System with a Correlated and Topological Flat Band. *Nat. Comm.* **12**, 2732 (2021).

14. Zhang, C. *et al.* Visualizing delocalized correlated electronic states in twisted double bilayer graphene. *Nat. Comm.* **12**, 2516 (2021).

15. Chen, G. *et al.* Signatures of tunable superconductivity in a trilayer graphene moiré superlattice. *Nature* **572**, 215–219 (2019).

16. Lyu, B. *et al.* Tunable correlated Chern insulator and ferromagnetism in a moiré superlattice. *Nature* **579**, 56-61 (2020).

17. Williams, R. Liquid Crystals in an Electric Field. *Nature* **199**, 273–274 (1963).

18. Fradkin, E., Kivelson, S. A., Lawler, M. J. & Mackenzie, A. P. Nematic Fermi Fluids in Condensed Matter Physics Further. *Annu. Rev. Condens. Matter Phys.* **1**, 153–178 (2010).

19. Fernandes, R. M., Chubukov, A. V. & Schmalian, J. What drives nematic order in iron-based superconductors? *Nat. Phys.* **10**, 97–104 (2014).

20. Cao, Y. *et al.* Nematicity and Competing Orders in Superconducting Magic-Angle Graphene. *Science,* **372** 264-271 (2021).

21. Kerelsky, A. *et al.* Moiréless Correlations in ABCA Graphene. PNAS **118** (4) e2017366118 (2020).

22. Edelberg, D., Kumar, H., Shenoy, V., Ochoa, H. & Pasupathy, A. N. Tunable strain soliton networks confine electrons in Van der Waals materials. *Nat. Phys.* **16**, 1097–1102 (2020).

23. Haddadi, F., Wu, Q., Kruchkov, A. J. & Yazyev, O. V. Moiré Flat Bands in Twisted Double Bilayer Graphene. *Nano Lett.* **20**, 2410-2415 (2020).

24. Koshino, M. Band structure and topological properties of twisted double bilayer graphene. *Phys. Rev. B* **99**, 235406 (2019).

25. Samajdar, R. & Scheurer, M. S. Microscopic pairing mechanism , order parameter , and disorder sensitivity in moiré superlattices : Applications to twisted double-bilayer graphene. *Phys. Rev. B* **102**, 064501 (2020).

26. Yankowitz, M. *et al.* Band structure mapping of bilayer graphene via quasiparticle scattering quasiparticle scattering. *APL Mater.* **092503**, (2014).

27. Fernandes, R. M. & Venderbos, J. W. F. Nematicity with a twist : Rotational symmetry breaking in a moiré superlattice. *Sci. Adv.* **6**, eaba8834 1–9 (2020).

28. Bi, Z., Yuan, N. F. Q. & Fu, L. Designing flat bands by strain. *Phys. Rev. B* **100**, 035448 (2019).

29. Scheurer, M. S. & Samajdar, R. Pairing in graphene-based moiré superlattices. *Phys. Rev. Res.* **2**, 033062 (2020).

30. Venderbos, J. W. F. & Fernandes, R. M. Correlations and electronic order in a two-orbital honeycomb lattice model for twisted bilayer graphene. *Phys. Rev. B* **98**, 245103 (2018).

31. Dodaro, J. F., Kivelson, S. A., Schattner, Y., Sun, X. Q. & Wang, C. Phases of a phenomenological model of twisted bilayer graphene. *Phys. Rev. B* **98**, 075154 (2018).

32. Isobe, H., Yuan, N. F. Q. & Fu, L. Unconventional Superconductivity and Density Waves in Twisted Bilayer Graphene. *Phys. Rev. X* **8**, 041041 (2018).

33. Kozii, V., Isobe, H., Venderbos, J. W. F. & Fu, L. Nematic superconductivity stabilized by

density wave fluctuations : Possible application to twisted bilayer graphene. *Phys. Rev. B* **99**, 144507 1–15 (2019).

34. Chichinadze, D. V, Classen, L. & Chubukov, A. V. Nematic superconductivity in twisted bilayer graphene. *Phys. Rev. B* **101**, 224513 1–18 (2020).

35. Kennes, D. M., Lischner, J. & Karrasch, C. Strong correlations and d + id superconductivity in twisted bilayer graphene. *Phys. Rev. B* **98**, 241407 (2018).

36. Soejim, T., Parker, D. E., Bultinck, N. & Hauschild, Johannes Zaletel, M. P. Efficient simulation of moire materials using the density matrix renormalization group. *Phys. Rev. B* **102***,* 205111 (2020).

37. Kang, J. & Vafek, O. Non-Abelian Dirac node braiding and near-degeneracy of correlated phases at odd integer fillingin magic-angle twisted bilayer graphene. *Phys. Rev. B* **102**, 035161 (2020).

38. Samajdar, R. *et al.* Electric-field-tunable electronic nematic order in twisted double-bilayer graphene. *2D Mater.* (2021).

39. Klebl, L., Kennes, D. M. & Honerkamp, C. Functional renormalization group for a large moiré unit cell. *Phys. Rev. B* **102**, 085109 (2020).

40. Girit, Ç. Ö. & Zettl, A. Soldering to a single atomic layer. *Appl. Phys. Lett.* **91**, 193512 (2007).

Figure Captions

Fig. 1. LDOS in twisted double bilayer graphene. a, STM topography on 1.05° TDBG (scale bar represents 100 nm, setpoint: 0.5 V, 30 pA). **b**, Zoomed-in image of an STM topograph and three-dimensional representation of the method used to obtain the heterostrain values. Following Ref. 4, we fitted a Gaussian function to the maximum of each BAAC site, thus obtaining the three moiré wavelengths as indicated with the black arrows. Setpoint: 0.5 V, 30 pA **c**, dI/dV at zero gate voltage on BAAC, ABCA and ABAB sites in 1.05° TDBG. Setpoint: 0.3 V, 250 pA. **d**-**e**, Tight-binding and continuum model calculations of the LDOS on BAAC, ABCA and ABAB sites. **f**, LDOS map at the energies indicated in panel c at zero doping. The three inequivalent sites are indicated by the circles. Setpoint: 0.3 V, 150 pA. **g**, Tight-binding simulations of the LDOS at the energies indicated in d. The moiré unit cell is indicated in white. Scale bars in b, f, g correspond to 10 nm. Curves are offset for clarity.

Fig. 2. Broken C_3 symmetry. a, dI/dV maps at the energy, doping and displacement field conditions indicated. **b**, LDOS map at the energy of the VFB and at the gate voltage in which broken rotational symmetry is observed. The three inequivalent lattice sites are shown as well as the moiré unit cells (dashed lines). **c**, dI/dV spectra on the three inequivalent sites at the doping conditions shown in a. The black dots indicate the energy position of the valence flat band on the different sites. Each spectrum is normalized to its value at the VFB maximum to facilitate comparison of the flat band energies between spatially distinct sites of the moiré lattice. **d,** dI/dV averaged over BAAC, ABAB and ABCA sites at the doping conditions shown in a. The color scale represents the anisotropy values obtained following Ref.4. Curves are offset for clarity. Setpoint for all panels: 0.3 V, 150 pA.

Fig. 3. Manifestations of long-range nematic order in TDBG. a, dI/dV maps at the energy of the valence flat band **a**, close to charge neutrality and **b**, around half-filling of the conduction flat band. The insets show the FFT of each LDOS map. The scale bar corresponds to 50 nm. Setpoint: 0.3 V, 150 pA. **c**-**d**, Energy evolution of the normalized intensity of the three moiré Bragg peaks. The first and second Brillouin zones are shown in the inset as well as the average spectrum over the regions shown in a and b. Dashed lines indicate the energy of the maps shown in a and b. **e**, Bragg peaks' intensity from the continuum model LDOS maps at the valence and conduction flat bands' energies. Each of the six panels maps the evolution of the Bragg peak with heterostrain strength and strain angle, which is defined with respect to the horizontal of the LDOS maps. **f**, Continuum model LDOS maps at the energy of the valence and conduction flat bands under the presence of 0.05 % strain at 20° strain angle.

Fig. 4. Moiré nematic order. **a**, TDBG schematic. The red sphere represents the range of interactions included in the tight-binding calculation. **b**, Tight-binding LDOS map corresponding to the competing instability that spontaneously breaks rotational symmetry. **c**-**d**, Twisted double bilayer graphene moiré patterns under the presence of moiré and graphene nematic order parameters, respectively. **e**, Non-interacting, moiré nematic and graphene nematic continuum model LDOS. The experimental STS LDOS at around half-filling of the conduction band is shown for comparison. The black dots indicate the energy position of the valence flat band. **f**-**h**, From top to bottom, the rows correspond to unperturbed, moiré nematic and graphene nematic continuum model LDOS maps, respectively. The energies and band correspondence of each LDOS map are included (valence and conduction flat bands VFB, CFB; remote valence and conduction bands RV_1, RC_1). The Fermi level is at 0.475 n_s of the conduction band to match the experiments. The moiré unit cell is shown in white.

Methods

We fabricated TDBG samples following the tear-and-stack method. PPC was used as a polymer to pick up hBN, then half of a piece of bilayer graphene, followed by the second half twisted relative to the first half. Then, we flipped over the structure and placed it on top of a Si/SiO2 chip. We made direct contact to the TDBG structure via microsoldering with Field's metal[40].
Ultra high-vacuum Scanning Tunneling Microscopy and Spectroscopy were carried out in a home-built STM at 5 K. Tungsten tips were prepared on clean Au(111) surface and calibrated to be atomically sharp and to detect the Au(111) Shockley surface state via STS.

STS LDOS maps were obtained in the following way. With the feedback loop open, the tip is placed on the desired position in constant current mode. Then, the feedback loop is closed, and the bias is swept in constant-height mode. Once the dI/dV curve is finished, the feedback loop is open again and the tip moves to the next position in constant current mode.

Data availability

The data represented in Figs. 1c,d, 2c,d, 3c,d and 4e are available as source data with the online version of the paper. All data that support the plots in this paper are available from the corresponding author upon reasonable request.

Code availability

All relevant source code is available from the corresponding author upon reasonable request.

Acknowledgements

S.T. and A.N.P. acknowledge funding from Programmable Quantum Materials, an Energy Frontier Research Center funded by the US Department of Energy (DOE), Office of Science, Basic Energy Sciences (BES), under award no. DE-SC0019443. STM equipment support (A.N.P.) and 2D sample synthesis (Y.S.) were provided by the Air Force Office of Scientific Research via grant no. FA9550-16-1-0601. C.R.-V. acknowledges funding from the European Union Horizon 2020 Research and Innovation Programme under the Marie Skłodowska-Curie grant agreement no. 844271. A.R. acknowledges funding by the European Research Council (ERC-2015-AdG-694097), Grupos Consolidados (IT1249-19) and the Flatiron Institute, a division of the Simons Foundation. L.K., D.M.K. and A.R. acknowledge funding by the Deutsche Forschungsgemeinschaft (DFG) under Germany's Excellence Strategy-Cluster of Excellence Matter and Light for Quantum Computing (ML4Q) EXC 2004/1-390534769 and Advanced Imaging of Matter (AIM) EXC 2056–390715994 and funding by the Deutsche Forschungsgemeinschaft (DFG) under RTG 1995, within the Priority Program SPP 2244 '2DMP' and GRK 2247. A.R. acknowledges support by the Max Planck Institute-New York City Center for Non-Equilibrium Quantum Phenomena. H.O. is supported by the NSF MRSEC programme grant no. DMR-1420634. Tight-binding and fRG simulations were performed with computing resources granted by RWTH Aachen University under projects rwth0496 and rwth0589. R.S. and M.S.S. acknowledge support from the National Science Foundation under grant no. DMR-2002850. R.M.F. was supported by the DOE-BES under award no. DE-SC0020045. K.W. and T.T. acknowledge support from the Elemental Strategy Initiative conducted by the MEXT, Japan (grant no. JPMXP0112101001), JSPS KAKENHI (grant no. JP20H00354) and the CREST (grant no. JPMJCR15F3) JST.

Author contributions

C.R.V. and S.T. performed the STM measurements. L.S. fabricated the samples for STM measurements. C.R.V. and S.T. performed experimental data analysis. K.W. and T.T. provided hBN crystals. L.K. L.X. and D.M.K. performed tight-binding calculations. S.T., R.S., M.S.S., J.W.F.V., H.O. and R.M.F. performed continuum-model calculations. R.M.F., A.R. and A.N.P. advised. C.R.V. and S.T. wrote the manuscript with assistance from all authors.

Corresponding author

Competing interests declaration

The authors declare no competing interests.

Additional information

Supplementary Information includes: 1. Continuum model LDOS under an external displacement field, 2. Direct evidence of primary nematic order, 3. Tight-binding model, 4. Functional Renormalization Group, 5. Nematic instability within the continuum model, 6. The effect of strain on the LDOS, 7. STS LDOS maps at charge neutrality and around half-filling, 8. Full energy range for large STS LDOS maps.

Figure 1

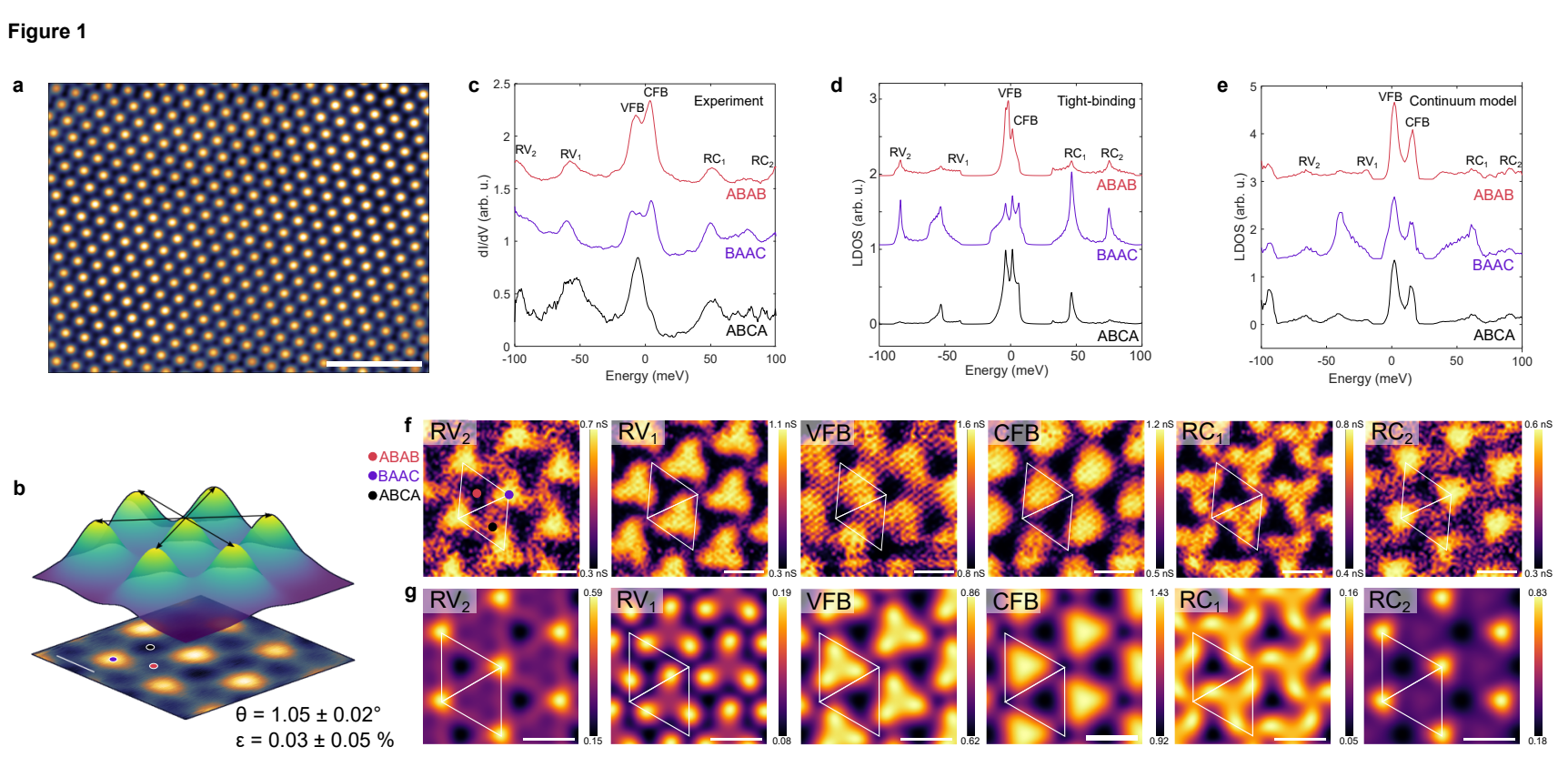
a
c
Experiment
CFB
VFB
RV2
RV1
RC1
RC2
ABAB
BAAC
ABCA
dI/dV (arb. u.)
Energy (meV)
d
Tight-binding
LDOS (arb. u.)
e
Continuum model
b
θ = 1.05 ± 0.02°
ε = 0.03 ± 0.05 %
f
g
ABAB
BAAC
ABCA
0.7 nS
0.3 nS
1.1 nS
1.6 nS
0.8 nS
1.2 nS
0.5 nS
0.4 nS
0.6 nS
0.59
0.15
0.19
0.08
0.86
0.62
1.43
0.92
0.16
0.05
0.83
0.18

Figure 2

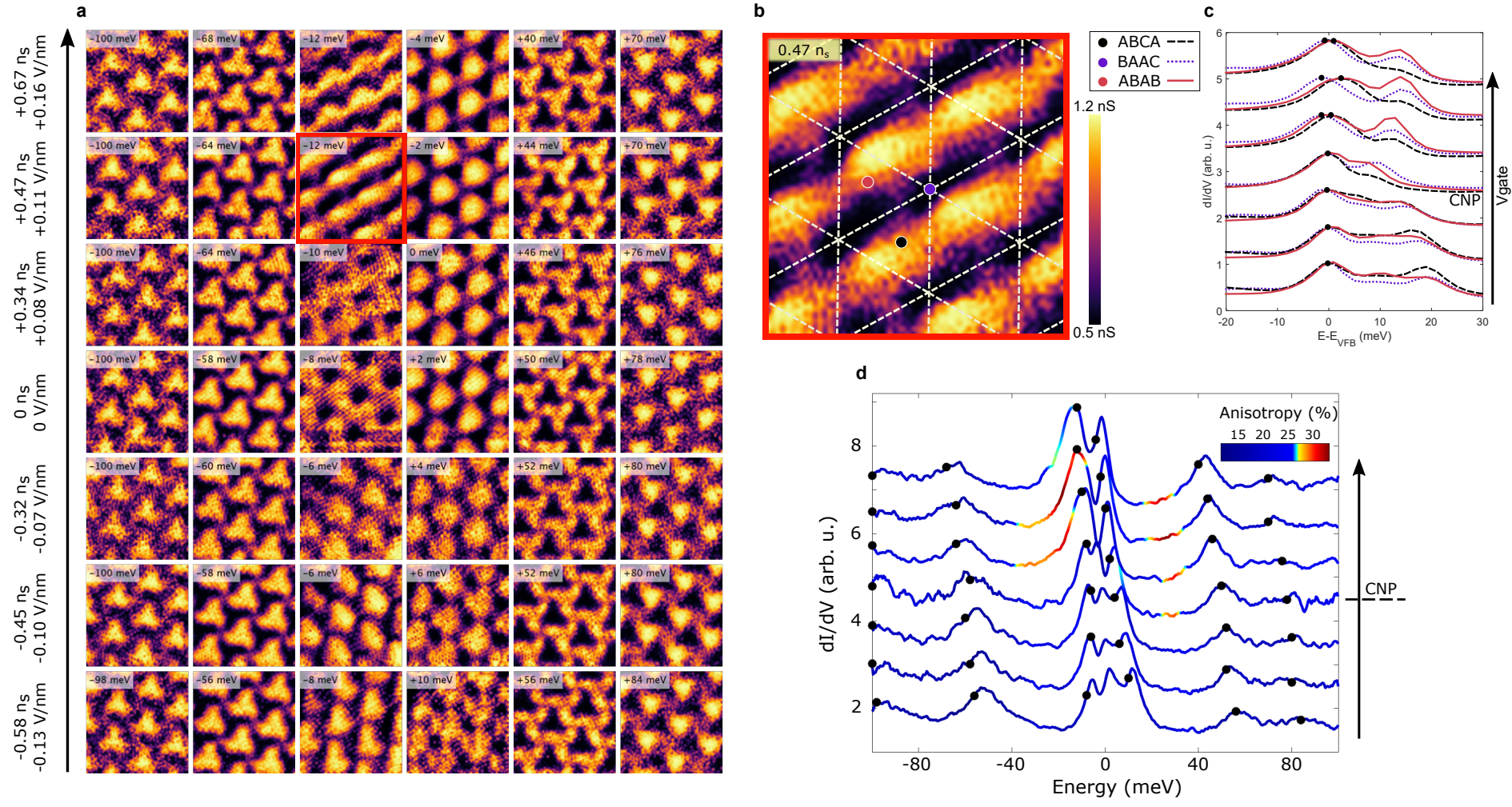
a
+0.67 ns
+0.16 V/nm
+0.47 ns
+0.11 V/nm
+0.34 ns
+0.08 V/nm
0 ns
0 V/nm
-0.32 ns
-0.07 V/nm
-0.45 ns
-0.10 V/nm
-0.58 ns
-0.13 V/nm
b
0.47 n_s
1.2 nS
0.5 nS
ABCA
BAAC
ABAB
c
dI/dV (arb. u.)
CNP
Vgate
E-E_VFB (meV)
d
Anisotropy (%)
15 20 25 30
dI/dV (arb. u.)
CNP
Energy (meV)

Figure 3

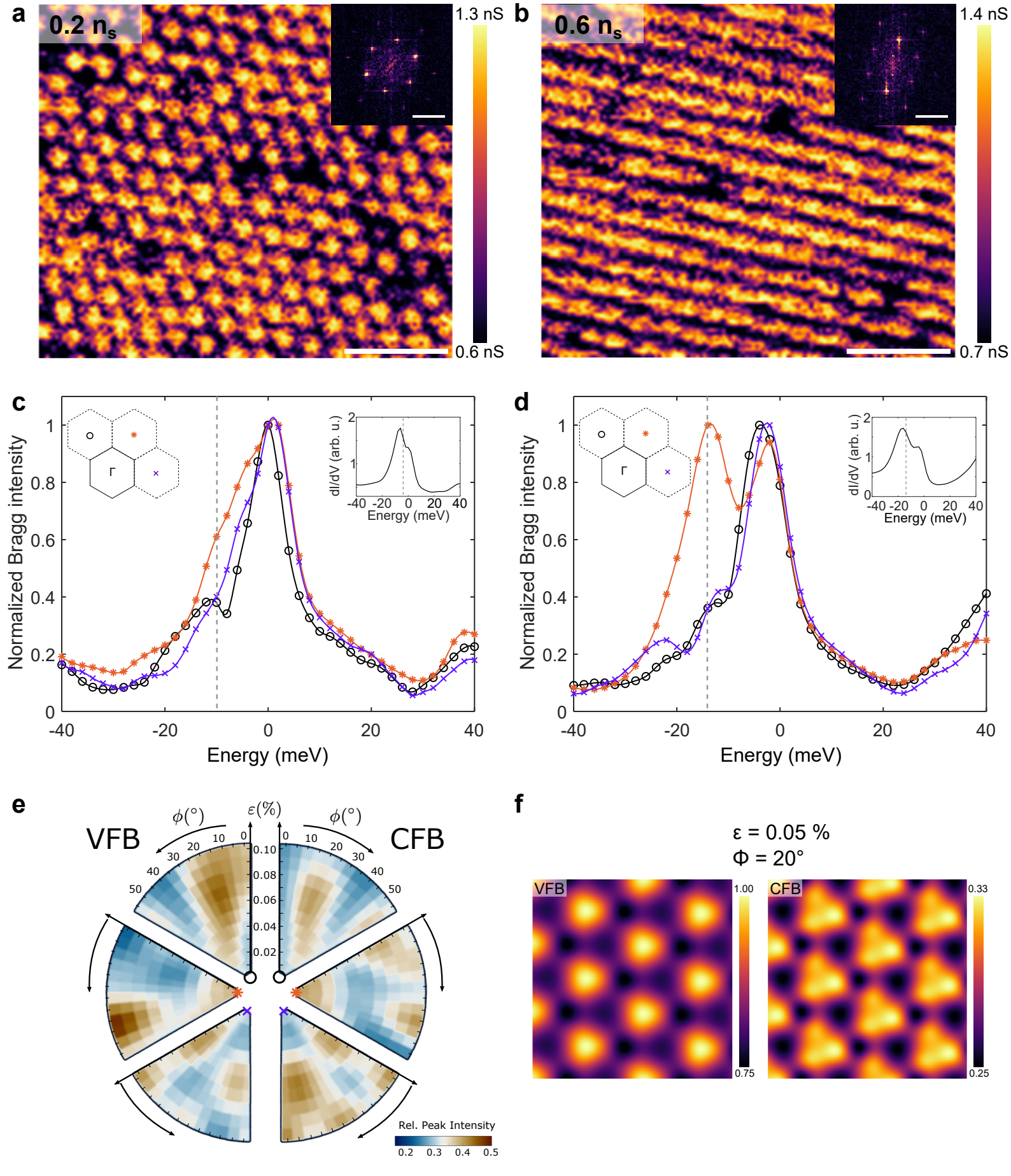
a
0.2 n_s
1.3 nS
0.6 nS
b
0.6 n_s
1.4 nS
0.7 nS
c
Normalized Bragg intensity
Energy (meV)
dI/dV (arb. u.)
Γ
d
Normalized Bragg intensity
Energy (meV)
dI/dV (arb. u.)
Γ
e
VFB
CFB
ϕ(°)
ε(%)
Rel. Peak Intensity
f
ε = 0.05 %
Φ = 20°
VFB
CFB

Figure 4

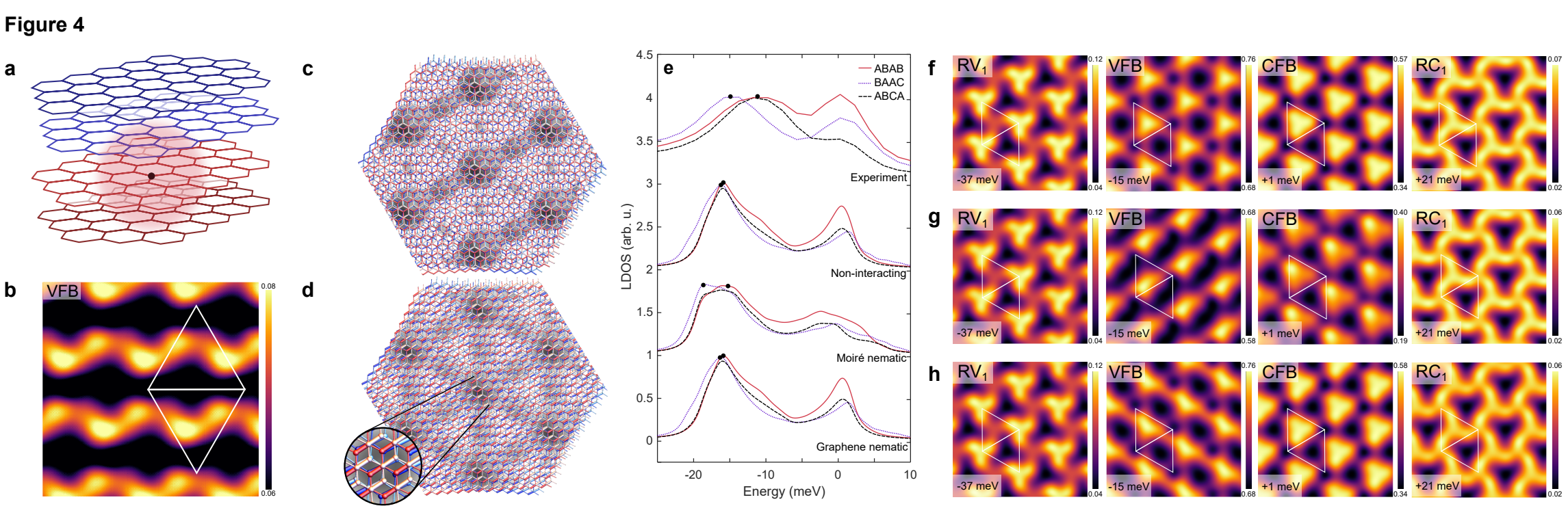
a
b
VFB
0.08
0.06
c
d
e
ABAB
BAAC
ABCA
Experiment
Non-interacting
Moiré nematic
Graphene nematic
LDOS (arb. u.)
Energy (meV)
f
g
h
RV1
VFB
CFB
RC1
-37 meV
-15 meV
+1 meV
+21 meV